Journal of Stress Analysis
Vol. 3, No. 1, Spring – Summer 2018
Bu-Ali Sina University

Effect of Interlaminar Weak Bonding and Constant Magnetic Field on the Hygrothermal Stresses of a FG Hybrid Cylindrical Shell Using DQM

M. Saadatfar*
Mechanical Engineering Department, University of Qom, Qom, Iran.

Article info

Article history:
Received 31 May 2018
Received in revised form
10 September 2018
Accepted 11 September 2018

Keywords:
Bonding imperfection
Hygrothermal
Magnetic field
Functionally graded hybrid shell

Abstract

In the present article, the influences of interlaminar bonding imperfection and constant magnetic field, as well as hygrothermal environmental conditions, on the stresses and displacements of a cylindrical shell with surface bounded sensor and actuator are investigated. The multiphysics analysis was carried out to explore the effects of moisture, temperature, electrical and mechanical loadings as well as magnetic field. The shell was simply supported and could be rested on an elastic foundation. The material properties of the shell and piezoelectric sensor and actuator were assumed to be functionally graded in the radial direction according to power-law function. Using the Fourier series expansion method through the longitudinal direction and the differential quadrature method (DQM) across the radial direction, governing differential equations were solved. The validity of the present work was verified by comparisons with other published works. Numerical results are presented to illuminate the effects of aspect ratio of shell and magnetic field on the responses of the hybrid shell.

Nomenclature

a, b, c, d	Radiuses of hybrid shell	u	Displacement
T	Temperature	C	Moisture concentration
k	Thermal conductivity coefficients	ζ	Moisture diffusivity coefficients
A_{ij}, B_{ij}	Weighting coefficients for DQM	E	Young's modulus
α	Coefficient of thermal expansion	σ_i	Stress
ε_i	Strain	E_i	Electric fields
C_{ij}	Elastic constants	e_{ij}	Piezoelectric constants
g_{ij}	Dielectric constants	λ_i	Thermal modulus
$\bar{w}_i$	Hygroscopic stress constants	P_1	Pyroelectric constant
P_2	Hygroelectric coefficient	ψ	Electric potential
$\vec{H}$	Magnetic intensity vector	$\vec{J}$	Electric current density vector
k_L	Winkler spring stiffness	μ	Magnetic permeability
D_i	Electric displacement	ξ	Moisture expansion coefficients

*Corresponding author: M. Saadatfar (Assistant Professor)
E-mail address: m.saadatfar@gmail.com
http://dx.doi.org/10.22084/jrstan.2018.16483.1051
ISSN: 2588-2597

$\mathcal{X}^k, \mathcal{X}T^k,$ $\mathcal{X}C^k$	Elastic, thermal and hygroscopic compliance constants of imperfect interface, respectively	β, η	Inhomogeneity index of FGPM and FGM layer, respectively
$\vec{h}$	Perturbation of the magnetic field vector		

1. Introduction

The performance advantages of the functionally graded material (FGM) together with the intrinsic ability of piezoelectric materials can be combined by considering smart structures including FGMs host members bonded with piezoelectric sensors or actuators. These smart structures are practically very important as they are related to vibration control, health monitoring, thermal stress control, and other engineering fields. Thus, the ability to predict the behavior of smart structures in multiphysics environmental conditions and under multifield loads is interesting for engineers and researchers [1-5].

Moreover, FGMs and laminated composites are increasingly used in the structural components of aircrafts and space vehicles that have severe hygrothermal conditions and in magnetic storage elements, plasma physics and the corresponding measurement methods of magneto-thermo-elasticity [6]. Besides, considering piezoelectric materials, an applied hygrothermal load leads to electrical polarization and mechanical displacement in the uncoupled hygrothermopiezoelectricity analysis [7]. Hygrothermo piezoelectric media have practical application in the presence of an external magnetic field in geophysics, optics, and acoustics. Therefore, the influence of multiple fields, such as moisture, temperature, magnetic, electric, and mechanical field should be considered in the multiphysics analysis. This analysis is a critical step for smart structures to several applications involving structural health monitoring, intelligent structures, energy harvesting and green energy production, optics, space vehicles, and self-powered biomedical devices [8].

Many researches have been conducted in the area of hygrothermal analysis of FGM and piezoelectric media. The hygrothermal analysis of FGM plates was presented by Zenkour [9]. A new higher order shear and normal deformation theory was developed to simulate the thermoelastic bending of FGM sandwich plates by Houari et al. [10]. Bellifa et al. [11] presented a new first-order shear deformation theory for bending and dynamic behaviors of functionally graded plates. Bakhshizadeh et al. [12] analyzed time-dependent hygrothermal creep behavior of pressurized FGM rotating thick cylindrical shells subjected to uniform magnetic field. Sobhy and Alotebi [13] carried out transient hygrothermal analysis of FG sandwich plates lying on a visco-pasternak foundation via a simple and accurate plate theory. Using the discrete-layer finite element method, Smittakorn and Heyliger [14] investigated the hygrothermo piezoelectric behavior of laminated plates. The hygrothermo elastic analysis of inhomogeneous piezoelectric and exponentially graded cylinders were carried out by Zenkour [15]. Wang et al. [16] analyzed the hygrothermal effects on the dynamic interlaminar stresses in laminated plates with piezoelectric actuator layers. Aeroelastic performances of smart composite plates under aerodynamic loads were investigated in hygrothermal environment by Mahato and Maiti [17]. The hygrothermal analysis in one-dimensional functionally graded piezoelectric media in a constant magnetic field was conducted by Akbarzadeh and Chen [18]. Zenkour [19] presented analytical solutions of hygrothermal effects in heterogeneous piezoelectric solid and hollow cylinders.

Furthermore, imperfect bonding is critical in hybrid laminates because of the high transverse stresses developed at the elastic-piezoelectric interfaces under an electric potential loading. Saadatfar and Aghaie-Khafri [20] showed that the actuation and sensing authority of smart layers were extensively affected by the multiphysical imperfection at the interfaces. It was observed that increasing the compliance coefficient of the imperfection results in reduction in the actuation capability of the actuator. Therefore, it is essential to study the effect of multiphysical bonding imperfection in hygrothermal condition for an accurate prediction of the structural behavior. Talebitooti et al. [21] studied the effects of imperfect bonding on sound transmission across a double-walled cylinder with FGM core using the three-dimensional theory of elasticity. Besides, actuators from functionally graded piezoelectric material (FGPM) could produce large displacements while minimizing the internal stress concentrations would greatly improve the reliability of distributed piezoelectric actuators and sensors. The application of FGPM layers as sensor and actuator in hybrid structures is rarely studied. Recently, Saadatfar and Aghaie-Khafri [22] presented an analytical solution for the magneto-thermo-electro-elastic problem of a long FGM cylindrical shell bonded to FGPM layers.

Some studies have been carried out on the thermoelastic analysis of the FG cylindrical shells bonded with piezoelectric layers. Alibeigloo [23] analyzed the deformation of a simply-supported FGM cylindrical shell with piezoelectric layers under thermo-mechanical loads. Using the DQ method, Akbari Alashti and Khorsand [24] presented static and dynamic analysis of FGM cylindrical shells with piezoelectric layers subjected to thermo-mechanical loads. Saadatfar and Aghaie-Khafri [25, 26] analyzed the magneto-thermo-electro-elastic problem of a short length FGM cylindrical shell bonded to FGPM layers. Saadatfar and

Aghaie-Khafri [27] studied the hygrothermal stress in functionally graded hybrid shell. Alibeigloo [28] investigated bending behavior of functionally graded carbon nanotube reinforced cylindrical composite panel attached to thin piezoelectric layers subjected to thermal-mechanical loads and electric field. Shaban and Alibeigloo [29] presented analytical solution for corrugated sandwich panels with embedded piezoelectric using three-dimensional theory of elasticity. Saadatfar [30] presented the hygrothermal stress analysis for FGM cylindrical shell with FGPM layer placed in a constant magnetic field. The material properties of FGM and FGPM layers were assumed to be exponentially graded in the radial direction.

It is well-known that by using the power law variation form, more general variation forms can be achieved rather than the exponential form for gradient of material properties of FGMs [31, 32]. Besides, more desirable behavior was reported for FGMs with power law form [33]. Particularly, to achieve the desired behavior, the effect of gradient index on the behavior of FGM cylindrical shell is more significant for power law form [34]. So, the power law variation form is more general and more applicable than exponentially form for material properties of FGMs. However, to the best of the authors' knowledge, the multiphysics hygrothermo-electro-elastic analysis of an FGM cylindrical shell imperfectly bonded with FGPM layers placed in a constant magnetic field has not yet been reported. In the present study, the material properties of the FGM shell and radially polarized FGPM layers were assumed to be graded in the radial direction according to the power law function. However, Poisson's ratio was assumed to be constant. The highly coupled partial differential equations were reduced to ordinary differential equations with variable coefficients by means of trigonometric function expansion in longitudinal directions. Then, the DQM was used across the thickness direction to solve the resulting equations.

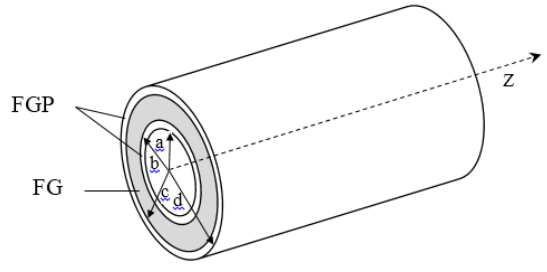

Fig. 1. FGM hollow cylinder with FGPM layers.

2. Basic Equations

An axisymmetric FGM shell with the inner and outer surfaces bonded FGPM layers was considered (Fig. 1). Due to the symmetry of the shell geometry and the boundary conditions, the moisture concentration, temperature, mechanical and electrical fields were assumed to be independent of the circumferential coordinate. The shell material was FGM and isotropic. Furthermore, the FGPM layer was transversely isotropic and the radial direction was the axis of the transverse isotropy.

2.1. Hygrothermal Problem Equations

The two physical fields, namely moisture and temperature, were obtained independently in an uncoupled hygrothermal problem [35]. The axisymmetric steady-state Fourier heat conduction and Fickian moisture diffusion equations without source of heat and moisture were considered as [20]:

$$\frac{1}{r}\frac{\partial}{\partial r}\left(rk_r\frac{\partial T}{\partial r}\right)+\frac{\partial}{\partial z}\left(k_z\frac{\partial T}{\partial z}\right)=0 \tag{1a}$$

$$\frac{1}{r}\frac{\partial}{\partial r}\left(r\zeta_r\frac{\partial C}{\partial r}\right)+\frac{\partial}{\partial z}\left(\zeta_z\frac{\partial C}{\partial z}\right)=0 \tag{1b}$$

where T and C represent the temperature and moisture concentration and k_r and k_z are the thermal conductivity coefficients and ζ_r and ζ_z are moisture diffusivity coefficients in the radial and longitudinal directions. The boundary conditions for the temperature field are:

$$\begin{aligned} &T_j(r,0)=T_j(r,L)=0, \qquad j=i,f,o\\ &T_i(a,z)=T_a, \qquad T_o(d,z)=T_d, \end{aligned} \tag{2}$$

and the boundary conditions for the moisture concentration are:

$$\begin{aligned} &C_j(r,0)=C_j(r,L)=0, \qquad j=i,f,o\\ &C_i(a,z)=C_a, \quad C_o(d,z)=C_d \end{aligned} \tag{3}$$

where the subscript $i, f,$ and o indicate the corresponding parameters in inner FGPM, FGM, and outer FGPM layer, respectively. The solutions of the hygrothermal problem that are governed by Eqs. (1-3) and satisfy temperature and moisture concentration boundary conditions at the end faces are:

$$T_j=\sum_{n=1}^{\infty}\bar{T}_{jn}(r)\sin(p_nz), \qquad j=i,f,o \tag{4a}$$

$$C_j=\sum_{n=1}^{\infty}\bar{C}_{jn}(r)\sin(p_nz), \qquad j=i,f,o \tag{4b}$$

where $p_n=\dfrac{n\pi}{L}$. The power law variation is assumed for all of material constants of FGPM layers as:

$$Y=\dot{Y}\left(\frac{r}{r_i}\right)^{\gamma}, \qquad \gamma=\beta_i,\beta_o \tag{5}$$

where Y and $\dot{Y}$ are material properties and corresponding magnitudes in the inner surface of each FGPM layer and β_i and β_o are inhomogeneity index for the inner and outer FGPM layer. Moreover, the power law variation is assumed for the Young's modulus, coefficient

of thermal expansion, magnetic permeability, moisture diffusivity coefficient, thermal conductivity constant and coefficient of the moisture concentration of FGM as:

$$E = E_f\left(\frac{r}{b}\right)^{\eta_1}, \quad \alpha = \alpha_f\left(\frac{r}{b}\right)^{\eta_2}, \quad \mu = \mu_f\left(\frac{r}{b}\right)^{\eta_3}$$
$$\zeta = \zeta_f\left(\frac{r}{b}\right)^{\eta_4}, \quad k = k_f\left(\frac{r}{b}\right)^{\eta_5}, \quad \xi = \xi_f\left(\frac{r}{b}\right)^{\eta_6} \tag{6}$$

where subscript f denotes the material properties in the inner surface of the FGM layer and $\eta_i s$ are their grading parameters. Poisson's ratio was taken to be constant through the shell thickness. Using Eqs. (4-6), Eqs. (1) are obtained as:

$$\left(k_{rj}\left(\frac{1+\gamma}{r}\frac{d\bar{T}_j}{dr} + \frac{d^2\bar{T}_j}{dr^2}\right) - k_{zj}p_n^2\bar{T}_j\right) = 0, \quad j = i, f, o \quad \gamma = \beta_i, \beta_o, \eta_5 \tag{7a}$$

$$\left(\zeta_{rj}\left(\frac{1+\gamma}{r}\frac{d\bar{C}_j}{dr} + \frac{d^2\bar{C}_j}{dr^2}\right) - \zeta_{zj}p_n^2\bar{C}_j\right) = 0, \quad j = i, f, o \quad \gamma = \beta_i, \beta_o, \eta_5 \tag{7b}$$

2.2. FGM Layer

The following relations can express stresses in the shell in terms of displacements, temperature field, and moisture concentration [27]:

$$\begin{aligned}
\sigma_r &= \frac{E(r)}{(1+\nu)(1-2\nu)}\left[(1-\nu)\varepsilon_r + \nu\varepsilon_\theta + \nu\varepsilon_z\right] \\
&\quad - \frac{E(r)}{1-2\nu}\left[\alpha(r)T(r,z) + \xi(r)C(r,z)\right] \\
\sigma_\theta &= \frac{E(r)}{(1+\nu)(1-2\nu)}\left[\nu\varepsilon_r + (1-\nu)\varepsilon_\theta + \nu\varepsilon_z\right] \\
&\quad - \frac{E(r)}{1-2\nu}\left[\alpha(r)T(r,z) + \xi(r)C(r,z)\right] \\
\sigma_z &= \frac{E(r)}{(1+\nu)(1-2\nu)}\left[\nu\varepsilon_r + \nu\varepsilon_\theta + (1-\nu)\varepsilon_z\right] \\
&\quad - \frac{E(r)}{1-2\nu}\left[\alpha(r)T(r,z) + \xi(r)C(r,z)\right] \\
\tau_{zr} &= \frac{E(r)}{2(1+\nu)}\gamma_{zr}
\end{aligned} \tag{8}$$

The strain-displacement relations are defined as:

$$\varepsilon_r = \frac{\partial u_r}{\partial r}, \quad \varepsilon_\theta = \frac{u}{r}, \quad \varepsilon_z = \frac{\partial u_z}{\partial_z}, \quad \gamma_{zr} = \left(\frac{\partial u_r}{\partial z} + \frac{\partial u_z}{\partial r}\right) \tag{9}$$

The shell was placed initially in an axial constant magnetic field. There was an interaction between deformation and perturbation of the magnetic field vector in the shell. Omitting displacement electric currents, the governing electrodynamic Maxwell equations for a perfectly conducting elastic body are given by [36]:

$$\vec{J} = \nabla \times \vec{h}, \quad \nabla \times \vec{e} = -\mu\frac{\partial \vec{h}}{\partial t}, \quad \mathrm{div}\vec{h} = 0$$
$$\vec{e} = -\mu\left(\vec{U}\frac{\partial \vec{U}}{\partial t} \times \vec{H}\right), \quad \vec{h} = \nabla \times (\vec{U} \times \vec{H}), \tag{10}$$

Where μ, $\vec{H}$, $\vec{J}$, and $\vec{h}$ are magnetic permeability (H/m), magnetic intensity vector, electric current density vector, and perturbation of the magnetic field vector, respectively. Equilibrium equations for axisymmetric deformations of the shell by taking into account the Lorentz's force are written as [37]:

$$\frac{\partial \sigma_r}{\partial r} + \frac{\partial \tau_{rz}}{\partial z} + \frac{\sigma_r - \sigma_\theta}{r} + f_r = 0$$
$$\frac{\partial \tau_{rz}}{\partial r} + \frac{\partial \sigma_z}{\partial z} + \frac{\tau_{rz}}{r} = 0 \tag{11}$$

where f_r is defined as the Lorentz's force. By applying an initial magnetic field vector in the cylindrical coordinate system to Eq. (10), the Lorentz's force can be written as:

$$\begin{aligned}
f_r &= \mu(\vec{J} \times \vec{H}) \\
&= \mu H^2\left(\frac{\partial^2 u_r}{\partial z^2} + \frac{1}{r}\frac{\partial u_r}{\partial r} - \frac{u_r}{r^2} + \frac{\partial^2 u_r}{\partial r^2}, 0, 0\right)
\end{aligned} \tag{12}$$

Using Eq. (8), Eqs. (11) can be rewritten as:

$$\frac{1}{(1+\nu)(1-2\nu)}\left(\left\{E\left[(1-\nu)\left(\frac{\partial^2}{\partial r^2} + \frac{1}{r}\frac{\partial}{\partial r} - \frac{1}{r^2}\right)\right] + \frac{\partial E}{\partial r}\left[(1-\nu)\frac{\partial}{\partial r} + \frac{\nu}{r}\right] + \frac{E(1-2\nu)}{2}\left[\frac{\partial}{\partial z^2}\right]\right\}u_r$$
$$+ \left\{\frac{E}{2}\frac{\partial^2}{\partial r \partial z} + \nu\frac{\partial E}{\partial r}\frac{\partial}{\partial z}\right\}u_z\Bigg) + \mu H^2\left(\frac{\partial^2 u}{\partial z^2} + \frac{1}{r}\frac{\partial u_r}{\partial r} - \frac{u_r}{r^2} + \frac{\partial^2 u}{\partial r^2}\right)$$
$$- \frac{1}{1-2\nu}\left(+\frac{dE}{dr}(\alpha T + \xi C) + E\left(\frac{d\alpha}{dr}T + \alpha\frac{\partial T}{\partial r} + \frac{d\xi}{dr}C + \xi\frac{\partial C}{\partial r}\right)\right) = 0 \tag{13a}$$

$$\frac{1}{2(1+\nu)}\left(\left\{\frac{E}{1-2\nu}\frac{\partial^2}{\partial r\partial z}+\left(\frac{E}{(1-2\nu)r}+\frac{1}{r}\frac{\partial E}{\partial r}\right)\frac{\partial}{\partial z}\right\}U_r+\left\{\frac{2E}{(1-2\nu)}\left[(1-\nu)\frac{\partial^2}{\partial z^2}\right]\right.\right.$$

$$\left.\left.+E\frac{\partial^2}{\partial r^2}+\left[\frac{E}{r}+\frac{1}{r}\frac{\partial E}{\partial r}\right]\frac{\partial}{\partial r}\right\}U_z\right)-\frac{E}{1-2\nu}\left(\alpha\frac{\partial T}{\partial z}+\xi\frac{\partial C}{\partial z}\right)=0 \tag{13b}$$

2.3. FGPM Layers

The constitutive relations describing the hygrothermal, electrical and mechanical interaction for a piezoelectric material are [27]:

$$\begin{aligned}
\sigma_r &= c_{11}\varepsilon_r + c_{12}\varepsilon_\theta + c_{13}\varepsilon_z - e_{11}E_r - \lambda_r T - \bar{w}_r C\\
\sigma_\theta &= c_{12}\varepsilon_r + c_{22}\varepsilon_\theta + c_{23}\varepsilon_z - e_{21}E_r - \lambda_\theta T - \bar{w}_\theta C\\
\sigma_z &= c_{13}\varepsilon_r + c_{23}\varepsilon_\theta + c_{33}\varepsilon_z - e_{31}E_r - \lambda_z T - \bar{w}_z C\\
\tau_{rz} &= c_{55}\gamma_{zr} - e_{53}E_z\\
D_r &= e_{11}\varepsilon_r + e_{21}\varepsilon_\theta + e_{31}\varepsilon_z + g_{11}E_r + P_1 T + P_2 C\\
D_z &= e_{53}\gamma_{zr} + g_{33}E_z
\end{aligned} \tag{14}$$

where σ_i, ε_i, D_i, and E_i represent stress, strain, electric displacement and electric fields, respectively. Cij, eij and gij denote the elastic, piezoelectric and dielectric constants, respectively. λ_i, $\bar{w}_i$, P_1 and P_2 are the thermal modulus, hygroscopic stress, pyroelectric constants and hygroelectric coefficient, respectively. The thermal stress and hygroscopic stress coefficients are related to the elastic coefficient, thermal expansion coefficient and moisture expansion coefficient as follows:

$$\begin{aligned}
\lambda_r &= c_{11}\alpha_r + c_{12}\alpha_\theta + c_{13}\alpha_z = \dot{\lambda}_r\left(\frac{r}{r_i}\right)^{2\beta}\\
\lambda_\theta &= c_{12}\alpha_r + c_{22}\alpha_\theta + c_{23}\alpha_z = \dot{\lambda}_\theta\left(\frac{r}{r_i}\right)^{2\beta}\\
\lambda_z &= c_{13}\alpha_r + c_{23}\alpha_\theta + c_{33}\alpha_z = \dot{\lambda}_z\left(\frac{r}{r_i}\right)^{2\beta}
\end{aligned} \tag{15a}$$

$$\begin{aligned}
\bar{w}_r &= c_{11}\xi_r + c_{12}\xi_\theta + c_{13}\xi_z = \dot{\bar{w}}_r\left(\frac{r}{r_i}\right)^{2\beta}\\
\bar{w}_\theta &= c_{12}\xi_r + c_{22}\xi_\theta + c_{23}\xi_z = \dot{\bar{w}}_\theta\left(\frac{r}{r_i}\right)^{2\beta}\\
\bar{w}_z &= c_{13}\xi_r + c_{23}\xi_\theta + c_{33}\xi_z = \dot{\bar{w}}_z\left(\frac{r}{r_i}\right)^{2\beta}
\end{aligned} \tag{15b}$$

Considering the electric potential Ψ, the electric field E is given by [23, 24]:

$$E_r = -\frac{\partial\psi}{\partial r}, \qquad E_z = -\frac{\partial\psi}{\partial z} \tag{16}$$

For the FGPM layers, in the absence of free charge density, the charge equation of electrostatics is [23, 24]:

$$\frac{1}{r}\frac{\partial}{\partial r}(rD_r)+\frac{\partial D_z}{\partial z}=0 \tag{17}$$

Using Eqs. (14-16), Eq. (11) and Eq. (17) can be written as:

$$\left(\dot{c}_{11}\frac{\partial^2}{\partial r^2}+\frac{(\beta+1)\dot{c}_{11}}{r}\frac{\partial}{\partial r}+\frac{\beta\dot{c}_{12}-\dot{c}_{22}}{r^2}+\dot{c}_{55}\frac{\partial^2}{\partial z^2}\right)u_r$$

$$+\left(\frac{1}{r}\big((\beta+1)\dot{c}_{13}-\dot{c}_{23}\big)\frac{\partial}{\partial z}+(\dot{c}_{13}+\dot{c}_{55})\frac{\partial}{\partial r\partial z}\right)u_z$$

$$+\left(\dot{e}_{11}\frac{\partial^2}{\partial r^2}+\frac{1}{r}\left(\big((\beta+1)\dot{e}_{11}-\dot{e}_{21}\big)\frac{\partial}{\partial r}\right)+\dot{e}_{53}\frac{\partial^2}{\partial z^2}\right)\psi$$

$$+\dot{\mu}H^2\left(\frac{\partial^2 u_r}{\partial z^2}+\frac{1}{r}\frac{\partial u_r}{\partial r}-\frac{u_r}{r^2}+\frac{\partial^2 u_r}{\partial r^2}\right)$$

$$+\left(\frac{r}{r_i}\right)^{\beta}\left[\left(\frac{1}{r}(\dot{\lambda}_\theta-(2\beta+1)\dot{\lambda}_r)-\dot{\lambda}_r\frac{\partial}{\partial r}\right)T\right.$$

$$\left.+\left(\frac{1}{r}(\dot{\bar{w}}_\theta-(2\beta+1)\dot{\bar{w}}_r)-\dot{\bar{w}}_r\frac{\partial}{\partial r}\right)C\right]=0 \tag{18a}$$

$$\left(\frac{1}{r}\left(\big((\beta+1)\dot{c}_{55}+\dot{c}_{23}\big)\frac{\partial}{\partial z}+(\dot{c}_{55}+\dot{c}_{13})\frac{\partial}{\partial r\partial z}\right)u_r\right.$$

$$+\left(\frac{\beta+1}{r}\dot{c}_{55}\frac{\partial}{\partial r}+\dot{c}_{55}\frac{\partial^2}{\partial r^2}+\dot{c}_{33}\frac{\partial^2}{\partial z^2}\right)u_z$$

$$+\left(\frac{\beta+1}{r}\dot{e}_{53}\frac{\partial}{\partial z}+(\dot{e}_{53}+\dot{e}_{31})\frac{\partial}{\partial r\partial z}\right)\psi$$

$$-\left(\frac{r}{r_i}\right)^{\beta}\frac{\partial}{\partial z}(\dot{\lambda}_z T+\dot{\bar{w}}_z C)=0 \tag{18b}$$

$$\left(\frac{(\beta+1)\dot{e}_{11}+\dot{e}_{21}}{r}\frac{\partial}{\partial r}+\beta\dot{e}_{21}\frac{1}{r^2}+\dot{e}_{11}\frac{\partial^2}{\partial r^2}+\dot{e}_{53}\frac{\partial^2}{\partial z^2}\right)u_r$$

$$+\left((\dot{e}_{53}+\dot{e}_{31})\frac{\partial}{\partial r\partial z}+\dot{e}_{31}\frac{\beta+1}{r}\frac{\partial}{\partial z}\right)u_z$$

$$-\left(\frac{(\beta+1)\dot{g}_{11}}{r}\frac{\partial}{\partial r}+\dot{g}_{11}\frac{\partial^2}{\partial r^2}+\dot{g}_{33}\frac{\partial^2}{\partial z^2}\right)\psi$$

$$+\left(\frac{\beta+1}{r}+\frac{\partial}{\partial r}\right)(\dot{P}_1 T+\dot{P}_2 C)=0 \tag{18c}$$

The simply supported and electrically insulated boundary conditions can be written as:

$$u_r = \sigma_z = \psi = 0 \qquad \text{at} \quad z = 0, L \tag{19}$$

Since the outer surface of the hybrid shell was assumed to be subjected to a Winkler elastic foundation, the surface boundary conditions can be considered as:

$$\begin{aligned} &\sigma_r = -p, \quad \tau_{zr} = 0, \quad \psi = V, \quad \text{at} \quad r = a \\ &\sigma_r = -k_L u_r, \quad \tau_{zr} = 0, \quad D_r = 0, \quad \text{at} \quad r = d \end{aligned} \tag{20}$$

where Winkler spring stiffness is indicated by k_L. Since imperfectly bonded interfaces may show extensive effects on the reliability of the designed smart layered structures, imperfections of bonded interfaces are also considered. The imperfect multiphysics interfacial conditions can be simulated by the generalized spring layer model [38]. For the imperfect interfaces, the displacements and moisture concentration as well as the temperature field at the interfaces may be discontinuous while the tractions at the interfaces, moisture flux, and the heat flux are always continuous. The following interfacial conditions are considered at the interfaces of all adjacent layers between k_{th} and $(k+1)_{th}$ interfaces:

$$\sigma_r|_{k+1} = \sigma_r|_k, \qquad \tau_{rz}|_{k+1} = \tau_{rz}|_k, \qquad \psi|_{k+1} = \psi|_k,$$

$$u_r|_{k+1} - u_r|_k = \mathcal{X}_r^k \sigma_r, \tag{21a}$$

$$u_z|_{k+1} - u_z|_k = \mathcal{X}_z^k, \tau_{rz},$$

$$k_r \frac{\partial T}{\partial r}\bigg|_{k+1} = k_1 \frac{\partial T}{\partial r}\bigg|_k, \quad T_{k+1} - T_k = \mathcal{X}_T^k k_r \frac{\partial T}{\partial r}\bigg|_{k+1} \tag{21b}$$

$$\zeta_r \frac{\partial C}{\partial r}\bigg|_{k+1} = \zeta_r \frac{\partial C}{\partial r}\bigg|_k, \quad C_{k+1} - C_k = \mathcal{X}_C^k \zeta_r \frac{\partial T}{\partial r}\bigg|_{k+1} \tag{21c}$$

$$k = 1, 2, \quad \text{at} \quad r = b, c$$

where $\mathcal{X}_i^k$ $(i = r, z)$, $\mathcal{X}_T^k$ and $\mathcal{X}_C^k$ are elastic, thermal and hygroscopic compliance constants of the imperfect interfaces. Obviously, for perfectly bonded interface there is: $\mathcal{X}_i^k$ $(i = r, z) = 0$, $\mathcal{X}_T^k = 0$ and $\mathcal{X}_C^k = 0$. A non-zero normal compliance coefficient, $\mathcal{X}_r^k$, characterizes the normal opening delamination, whereas the shear slip delamination is characterized by non-zero tangential compliance coefficients $\mathcal{X}_z^k$.

3. Solution of Governing Differential Equations

The solution satisfying the boundary conditions may be assumed as:

$$\begin{aligned} u_r &= \sum_{n=1}^{\infty} U_r(r) \sin(b_n z) \\ u_z &= \sum_{n=1}^{\infty} U_z(r) \cos(b_n z) \\ \psi &= \sum_{n=1}^{\infty} \Psi(r) \sin(b_n z) \end{aligned} \tag{22}$$

where $b_n = \dfrac{n\pi}{L}$. Substituting Eq. (22) into governing equations, partial differential equations are reduced to ordinary differential equations and governing equations for the FGM shell can be expressed as:

$$\begin{aligned} &\frac{1}{(1+\nu)(1-2\nu)} \Bigg(\Bigg\{ E \left[(1-\nu) \left(\frac{d^2}{dr^2} + \frac{1}{r}\frac{d}{dr} - \frac{1}{r^2} \right) \right] \\ &+ \frac{\partial E}{\partial r} \left[(1-\nu)\frac{d}{dr} + \frac{\nu}{r} \right] - b_n^2 \frac{E(1-2\nu)}{2} \\ &+ (1+\nu)(1-2\nu)\mu H^2 \left(-b_n^2 + \frac{1}{r}\frac{d}{dr} - \frac{1}{r^2} + \frac{d^2}{dr^2} \right) \Bigg\} U_r \\ &+ \left\{ -\frac{E b_n}{2}\frac{d}{dr} - \nu \frac{\partial E}{\partial r} b_n \right\} U_z \Bigg) \\ &- \frac{1}{1-2\nu} \left(\frac{d\alpha}{dr} E + \frac{dE}{dr}\alpha + E\alpha \frac{d}{dr} \right) \bar{T} \\ &- \frac{1}{1-2\nu} \left(\frac{d\xi}{dr} E + \frac{dE}{dr}\xi + E\xi \frac{d}{dr} \right) \bar{C} = 0 \end{aligned} \tag{23a}$$

$$\begin{aligned} &\frac{1}{2(1+\nu)} \Bigg(\left\{ \frac{E b_n}{1-2\nu}\frac{d}{dr} + \left(\frac{E}{(1-2\nu)r} + \frac{1}{r}\frac{\partial E}{\partial r} \right) b_n \right\} U_r \\ &+ \left\{ \frac{-2E}{(1-2\nu)} [(1-\nu) b_n^2] + E\frac{d^2}{dr^2} + \left[\frac{E}{r} + \frac{1}{r}\frac{\partial E}{\partial r} \right] \frac{d}{dr} \right\} U_z \Bigg) \\ &- \frac{E b_n}{1-2\nu} (\alpha \bar{T} + \xi \bar{C}) = 0 \end{aligned} \tag{23b}$$

and corresponding equations for the FGPM layers can be expressed as:

$$\begin{aligned} &\Bigg(\dot{c}_{11}\frac{d^2}{dr^2} + \frac{(\beta+1)\dot{c}_{11}}{r}\frac{d}{dr} + \frac{\beta \dot{c}_{12} - \dot{c}_{22}}{r^2} - \dot{c}_{55} b_n^2 \\ &+ \mu H^2 \left(-b_n^2 + \frac{1}{r}\frac{d}{dr} - \frac{1}{r^2} + \frac{d^2}{dr^2} \right) \Bigg) U_r \\ &- \left(\frac{b_n}{r}((\beta+1)\dot{c}_{13} - \dot{c}_{23}) + b_n(\dot{c}_{13} + \dot{c}_{55})\frac{d}{dr} \right) U_z \end{aligned}$$

$$+\left(\dot{e}_{11}\frac{d^2}{dr^2}+\frac{(\beta+1)\dot{e}_{11}-\dot{e}_{21}}{r}\frac{d}{dr}-\dot{e}_{53}b_n^2\right)\Psi$$

$$+\left(\frac{r}{r_i}\right)^{\beta}\left[\left(\frac{1}{r}(\dot{\lambda}_\theta-(2\beta+1)\dot{\lambda}_r)-\dot{\lambda}_r\frac{d}{dr}\right)\bar{T}\right.$$

$$\left.+\left(\frac{1}{r}(\dot{\bar{w}}_\theta-(2\beta+1)\dot{\bar{w}}_r)-\dot{\bar{w}}_r\frac{d}{dr}\right)\bar{C}\right]=0 \tag{24a}$$

$$\left\{\left(\frac{b_n}{r}((\beta+1)\dot{c}_{55}+\dot{c}_{23})+b_n(\dot{c}_{55}+\dot{c}_{13})\frac{d}{dr}\right)U_r\right.$$

$$\left(\frac{\beta+1}{r}\dot{c}_{55}\frac{d}{dr}+\dot{c}_{55}\frac{d^2}{dr^2}-\dot{c}_{33}b_n^2\right)U_z$$

$$\left.+\left(b_n\frac{\beta+1}{r}\dot{e}_{53}+b_n(\dot{e}_{53}+\dot{e}_{31})\frac{d}{dr}\right)\Psi\right\}$$

$$-b_n\left(\frac{r}{r_i}\right)^{\beta}(\dot{\lambda}_z\bar{T}+\dot{\bar{w}}_z\bar{C})=0 \tag{24b}$$

$$\left\{\left(\frac{(\beta+1)\dot{e}_{11}+\dot{e}_{21}}{r}\frac{d}{dr}+\frac{\beta\dot{e}_{21}}{r^2}+\dot{e}_{11}-\dot{e}_{53}b_n^2\right)U_r\right.$$

$$-\left(b_n(\dot{e}_{53}+\dot{e}_{31})\frac{d}{dr}+b_n\dot{e}_{31}\frac{\beta+1}{r}\right)U_z$$

$$\left.-\left(\frac{(\beta+1)\dot{g}_{11}}{r_i}\frac{d}{dr}+\dot{g}_{11}\frac{d^2}{dr^2}-\dot{g}_{33}b_n^2\right)\Psi\right\}$$

$$+\left(\frac{\beta+1}{r}+\frac{d}{dr}\right)(\dot{P}_1\bar{T}+\dot{P}_2\bar{C})=0 \tag{24c}$$

According to the DQM, the nth-order derivative of the function f(x) at any sample point can be approximated by the following formulation [39]:

$$\frac{d^n f(x_i)}{dx^n}=\sum_{j=1}^{N}A_{ij}^{(n)}f(x_j)$$
$$i=1,\cdots,N,\quad n=1,\cdots,N-1 \tag{25}$$

where A_{ij} are the weighting coefficients associate with the n_{th}-order derivatives, and N is the number of grid points in the x direction. Using the Lagrange interpolation polynomials as approximating functions, the following algebraic formulations can be used to compute the first and the second order weighting coefficients [39]:

$$A_{ij}^{(1)}=\frac{\prod(x_i)}{(x_i-x_j)\cdot\prod(x_j)}\quad i,j=1,\cdots,N \text{ and } j\neq i$$

$$A_{ij}^{(2)}=2\left[A_{ii}^{(1)}\cdot A_{ij}^{(1)}-\frac{A_{ij}^{(1)}}{x_i-x_j}\right]\quad 2\le n\le N-1$$

$$A_{ii}^{(1)}-\sum_{j=1,\ j\neq i}^{N}A_{ij}^{(1)}\quad k=1,\cdots,N-1$$

$$\prod(x_i)=\prod_{j=1,\ j\neq i}^{N}(x_i-x_j) \tag{26}$$

A significant factor for the accuracy of the DQ solution is the choice of the sampling or grid points. For the numerical computation, the Chebyshev–Gauss–Lobatto points with the following coordinates were used [39]:

$$x_i=\frac{L}{2}\left(1-\cos\left[\frac{(i-1)\pi}{(N-1)}\right]\right)\quad i=1,2,3,\cdots,N \tag{27}$$

Using the DQ technique, the equations of the FGM layer, FGPM layers, thermal and moisture concentration fields can be expressed as: FGM layer:

$$\frac{E_0\left(\frac{r}{b}\right)^{\eta_1}}{(1+\nu)(1-2\nu)}\left(\left\{\left[(1-\nu)\left(\sum_{j=1}^{N}B_{ij}^{(2)}+\frac{1}{r_i}\sum_{j=1}^{N}B_{ij}^{(1)}-\frac{1}{r_i^2}\right)\right]+\frac{\eta_1}{r_1}\left[(1-\nu)\sum_{j=1}^{N}B_{ij}^{(1)}+\frac{\nu}{r_i}\right]\right.\right.$$

$$\left.-b_n^2\frac{(1-2\nu)}{2}+\frac{(1+\nu)(1-2\nu)}{E_0}\mu_f H^2\left(\frac{r_i}{b}\right)^{\eta_3-\eta_1}\left(-b_n^2+\sum_{j=1}^{N}B_{ij}^{(2)}+\frac{1}{r}\sum_{j=1}^{N}B_{ij}^{(1)}-\frac{1}{r_i^2}\right)\right\}U_{rj}$$

$$+\left\{-\frac{b_n}{2}\sum_{j=1}^{N}B_{ij}^{(1)}-\nu\frac{\eta_1}{r_i}b_n\right\}U_{zj}-\alpha_0(1+\nu)\left(\frac{r_i}{b}\right)^{\eta_2}\left(\frac{\eta_2}{r_i}+\frac{\eta}{r_i}+\sum_{j=1}^{N}B_{ij}^{(1)}\right)\bar{T}$$

$$\left.-\xi_0(1+\nu)\left(\frac{r_i}{b}\right)^{\eta_6}\left(\frac{\eta_2}{r_i}+\frac{eta_1}{r_i}+\sum_{j=1}^{N}B_{ij}^{(1)}\right)\bar{C}\right)=0 \tag{28a}$$

$$\frac{E_0\left(\frac{r}{b}\right)^{\eta_1}}{1(1+\nu)}\left(\left\{\left[\frac{b_n}{1-2\nu}\left(\sum_{j=1}^{N}B_{ij}^{(2)}+\left(\frac{1}{(1-2\nu)r_i}+\frac{\eta_1}{r_i^2}\right)b_n\right\}U_{rj}+\left\{\frac{-2(1-\nu)}{(1-2\nu)}b_n^2+\sum_{j=1}^{N}B_{ij}^{(2)}\right.\right.\right.$$

$$\left.\left.\left.+\left(\frac{1}{r_i}+\frac{\eta_1}{r_i^2}\right)\sum_{j=1}^{n}B_{ij}^{(1)}\right\}U_{zj}\right)-\frac{E_f b_n}{1-2\nu}\left(\left(\frac{r_i}{b}\right)^{\eta_1+\eta_2}\alpha_f\bar{T}+\left(\frac{r_i}{b}\right)^{\eta_1+\eta_6}\xi_f\bar{C}\right)=0 \tag{28b}$$

FGPM layer:

$$\left((\dot{c}_{11}+\dot{\mu}H^2)\sum_{j=1}^{N}A_{ij}^{(2)}+\left(\frac{(\beta+1)\dot{c}_{11}+\dot{\mu}H^2}{r_i}\right)\sum_{j=1}^{N}A_{ij}^{(1)}+\frac{\beta\dot{c}_{12}-\dot{c}_{22}-\dot{\mu}H^2}{r_i^2}-(\dot{c}_{55}+\dot{\mu}H^2)b_n^2\right)U_{rj}$$

$$-\left(\frac{b_n}{r_i}((\beta+1)\dot{c}_{13}-\dot{c}_{23})+b_n^2(\dot{c}_{13}+\dot{c}_{55})\sum_{j=1}^{N}A_{ij}^{(1)}\right)U_{zj}+\left(\dot{e}_{11}\sum_{j=1}^{N}A_{ij}^{(2)}+\frac{(\beta+1)\dot{e}_{11}-\dot{e}_{21}}{r_i}\sum_{j=1}^{N}A_{ij}^{(1)}-\dot{e}_{53}b_n^2\right)\Psi_j$$

$$+\left(\frac{r_i}{b}\right)^{\beta}\left(\left(\frac{1}{r_i}(\dot{\lambda}_\theta-(2\beta+1)\dot{\lambda}_r)-\dot{\lambda}_r\sum_{j=1}^{N}A_{ij}^{(1)}\right)\bar{T}+\left(\frac{1}{r_i}(\dot{\bar{w}}_\theta-(2\beta+1)\dot{\bar{w}}_r)-\dot{\bar{w}}_r\sum_{j=1}^{N}A_{ij}^{(1)}\right)\bar{C}\right)=0 \tag{29a}$$

$$\left\{\left(\frac{b_n}{r_i}((\beta+1)\dot{c}_{55}+\dot{c}_{23})+b_n(\dot{c}_{55}+\dot{c}_{13})\sum_{j=1}^{N}A_{ij}^{(1)}\right)U_{rj}+\left(\frac{\beta+1}{r_i}\dot{c}_{55}\sum_{j=1}^{N}A_{ij}^{(1)}+\dot{c}_{55}\sum_{j=1}^{N}A_{ij}^{(2)}-\dot{c}_{33}b_n^2\right)U_{zj}\right.$$

$$\left.+\left(b_n\frac{\beta+1}{r_i}\dot{e}_{23}+b_n(\dot{e}_{53}+\dot{e}_{31})\sum_{j=1}^{N}A_{ij}^{(1)}\right)\Psi_j\right\}-b_n\left(\frac{r_i}{a}\right)^{\beta}(\dot{\lambda}_z\bar{T}+\dot{\bar{w}}_z\bar{C}=0 \tag{29b}$$

$$\left(\frac{(\beta+1)\dot{e}_{11}+\dot{e}_{21}}{r_i}\sum_{j=1}^{N}A_{ij}^{(1)}+\frac{\beta\dot{e}_{21}}{r_i^2}+\dot{e}_{11}\sum_{j=1}^{N}A_{ij}^{(2)}-\dot{e}_{53}b_n^2\right)U_{rj}-\left(b_n(\dot{e}_{53}+\dot{e}_{31})\sum_{j=1}^{N}A_{ij}^{(1)}+b_n\dot{e}_{31}\frac{\beta+1}{r_i}\right)U_{zj}$$

$$-\left(\frac{(\beta+1)\dot{g}_{11}}{r_i}\sum_{j=1}^{N}A_{ij}^{(1)}+\dot{g}_{11}\sum_{j=1}^{N}A_{ij}^{(2)}-\dot{g}_{33}b_n^2\right)\Psi_j\Bigg\}+\left(\frac{\beta+1}{r}+\sum_{j=1}^{N}A_{ij}^{(1)}\right)(\dot{P}_1\bar{T}+\dot{P}_2\bar{C})=0 \tag{29c}$$

Thermal and moisture concentration field:

$$\left(k_{rj}\left(\frac{1+\gamma}{r_i}\sum_{j=1}^{N}A_{ij}^{(1)}+\sum_{j=1}^{N}A_{ij}^{(1)}\right)-k_{zj}p_n^2\right)\bar{T}_i=0 \tag{30a}$$

$$\left(\zeta_{rj}\left(\frac{1+\gamma}{r_i}\sum_{j=1}^{N}A_{ij}^{(1)}+\sum_{j=1}^{N}A_{ij}^{(1)}\right)-\zeta_{zj}p_n^2\right)\bar{C}_i=0 \tag{30b}$$

In the above equations, A_{ij} and B_{ij} are weighting coefficients for FGPM and FGM layers, respectively. In a similar way, the boundary conditions can be discretized. So, the boundary conditions at $r=a$ and $r=d$ become:

$$\left[\left(\dot{c}_{11}\sum_{j=1}^{N}A_{ij}^{(1)}+\frac{\dot{c}_{12}}{a}\right)U_r-\dot{c}_{13}b_nU_z+\dot{e}_{11}\sum_{j=1}^{N}A_{ij}^{(1)}\Psi\right]$$

$$-\dot{\lambda}_r\bar{T}-\dot{\bar{w}}_r\bar{C}=-p,$$

$$\left[\dot{c}_{55}\left(b_nU_r+\sum_{j=1}^{N}A_{ij}^{(1)}U_z\right)+\dot{e}_{53}b_n\Psi\right]=0, \tag{31}$$

$$\Psi=V,$$

$$\left[\left(\dot{c}_{11}\sum_{j=1}^{N}C_{ij}^{(1)}+\frac{\dot{c}_{12}}{d}-(k_LU_r)\right)U_r-\dot{c}_{13}b_nU_z+\dot{e}_{11}\sum_{j=1}^{N}A_{ij}^{(1)}\Psi\right]$$

$$-\left(\frac{d}{c}\right)^{\beta}(\dot{\lambda}_r\bar{T}+\dot{\bar{w}}_r\bar{C})=0$$

$$\left[\dot{c}_{55}\left(b_nU_r+\sum_{j=1}^{N}A_{ij}^{(1)}U_z\right)+\dot{e}_{53}b_n\Psi\right]=0, \tag{32}$$

$$\left[\left(\dot{e}_{11}\sum_{j=1}^{N}A_{ij}^{(1)}+\frac{\dot{e}_{21}}{d}\right)U_r-\dot{e}_{31}b_nU_z-\dot{g}_{11}\sum_{j=1}^{N}A_{ij}^{(1)}\Psi\right]$$

$$+\dot{P}_1\bar{T}+\dot{P}_2\bar{C}=0, \tag{33}$$

Domain and boundary degrees of freedom were separated and in vector forms, they were denoted as (d) and (b), respectively. Based on this definition, the matrix form of governing equations and related boundary conditions take the following form:

$$\begin{bmatrix} [A_{bb}] & [A_{bd}] \\ [A_{db}] & [A_{dd}] \end{bmatrix} \begin{Bmatrix} \{U_b\} \\ \{U_d\} \end{Bmatrix} = \begin{Bmatrix} \{F_b\} \\ \{F_d\} \end{Bmatrix} \tag{34}$$

where,

$$\begin{aligned} \{U_b\} &= \{\{U_{rb}, \{U_{zb}\}, \{\psi_b\}\}^T \\ \{U_d\} &= \{\{U_{rd}, \{U_{zd}\}, \{\psi_d\}\}^T \end{aligned} \tag{35}$$

By eliminating the column vector $\{U_b\}$, the matrix Eq. (33) is reduced to the following system of algebraic equations:

$$[A]\{U_d\} = \{F\} \tag{36}$$

where,

$$\begin{aligned} [A] &= [A_{dd}] - [A_{db}][A_{bb}]^{-1}[A_{bd}] \\ \{F\} &= \{F_d\} - \{A_{db}\}[A_{bb}]^{-1}\{F_b\} \end{aligned} \tag{37}$$

Eq. (35) is a system of algebraic equations which can be solved using various direct or iterative methods. Since the size of resulting algebraic equations is large, the direct methods may not be efficient. Thus, iterative methods such as the Gauss–Seidel method were recommended for the solution of the resultant algebraic equations.

4. Numerical Results and Discussion

In this section, some numerical examples are considered to explore the effects of key parameters on the present analysis. The material properties of FGPM layers, as actuator and sensor layers, are assumed to be as listed in Table 1 [27]. Moreover, the material constants of the inner surface of the FGM layer are assumed to be: $E_0 = 125.83$(GPa), $\alpha_0 = 10\times10^{-6}$(1/K), $k_0 = 25$(W/mK), $\zeta_0 = 2.2 \times 10^{-8}$kg/(ms°M), $\xi_0 = 33 \times 10^{-5}$m^3/kg for Zirconia. However, the material constants of the outer surface are considered as: $E_h = 227.24$(GPa), $\alpha_h = 15 \times 10^{-6}$(1/K), $k_h = 2.09$(W/mK), $\zeta_h = 12.2 \times 10^{-8}$kg/(ms°M) and $\xi_h = 44 \times 10^{-5}$m^3/kg for Monel.

The material properties of the host shell were assumed to vary according to the power law and material properties parameters $\eta_1, \eta_2, \eta_4, \eta_5$ and η_6 are:

$$\eta_1 = \frac{\ln(E_h/E_0)}{\ln(c/b)},\ \eta_2 = \frac{\ln(\alpha_h/\alpha_0)}{\ln(c/b)},\ \eta_4 = \frac{\ln(\zeta_h/\zeta_0)}{\ln(c/b)},$$

$$\eta_5 = \frac{\ln(k_h/k_0)}{\ln(c/b)},\ \eta_6 = \frac{\ln(\xi_h/\xi_0)}{\ln(c/b)}$$

In this work, it was considered that $\eta_3 = 1$. It should be noted that 40 terms were considered in the series expansion and all numerical results were calculated and presented for the value of $z = L/2$. In all numerical simulations, unless otherwise stated, the values were $a = 0.9$m, $d = 1.1$m, $h_{FGM} = 20h_{FGPM}$ and $L = 6$m. The aspect ratio (S) of the shell was defined as: (middle radius)/(thickness of shell). Furthermore, the following dimensionless quantities are introduced:

$$R = \frac{r-a}{d-a}, \quad u_i^* = \frac{u_i(r)}{h_{FGM}} \quad (i = r, z),$$

$$\sigma_j^* = \frac{\sigma_j}{P}, \quad (j = r, \theta, z, rz), \quad T^* = \frac{T}{T_a}, \quad M^* = \frac{M}{M_a}.$$

To show the convergence and correctness of the present approach, numerical results for the static behavior of the FGM shell with homogeneous piezoelectric layers under thermomechanical boundary conditions are presented and compared with the results reported in Ref. [23, 24]. In this case, $\beta_i = \beta_o = k_L = H = 0$. Fig. 2 and Table 2 show a good agreement between the distribution of temperature and radial stress with the literature. It is obvious from Fig. 2b and Table 2 that by increasing the number of grid points, results of the DQ method converge rapidly and approach to the reported results.

Table 1
Materials constants.

Property (GPa)	$\dot{c}_{11}$	$\dot{c}_{12}$	$\dot{c}_{13}$	$\dot{c}_{22}$	$\dot{c}_{23}$	$\dot{c}_{33}$	$\dot{c}_{55}$	
Sensor	115	74	74	139	78	139	25.6	
Actuator	135	52	5	247	104	239	66	
Property*	$\dot{e}_{11}$	$\dot{e}_{21}$	$\dot{e}_{31}$	$\dot{e}_{53}$	$\dot{g}_{11}$	$\dot{g}_{33}$	$\dot{P}_1$	$\dot{P}_2$
Sensor	15.1	-5.2	-5.2	12.7	5.6	6.5	5.4	-2.5
Actuator	4.3	-0.3	-0.4	2.8	0.28	1.96	5.4	-2.5
Property*	$\dot{\alpha}_r$	$\dot{\alpha}_\theta = \dot{\alpha}_z$	$\dot{k}_\theta = \dot{k}_z$	$\dot{k}_r$	$\dot{\xi}_r$	$\dot{\xi}_\theta = \dot{\xi}_z$	$\dot{\zeta}_\theta = \dot{\zeta}_z = \dot{\zeta}_r$	$\dot{\rho}_p$
Sensor	2.62	1.99	2.1	0.8	1.1	430	7500	
Actuator	2.45	4.39	8.6	13.9	0.8	1.6	1731	5300

* The units are: e in C/m^2, g×10^{-9} in C^2/Nm^2, $P_1 \times 10^{-5}$ in C^2/m^{2}K, $P_2 \times 10^{-5}$ in Cm/kg, $\alpha \times 10^{-6}$ in 1/K, k in W/mK, $\xi \times 10^{-4}$ in m^{3}kg, $\zeta \times 10^{-11}$ in kg/(ms°M) and ρ in kg/m^3.

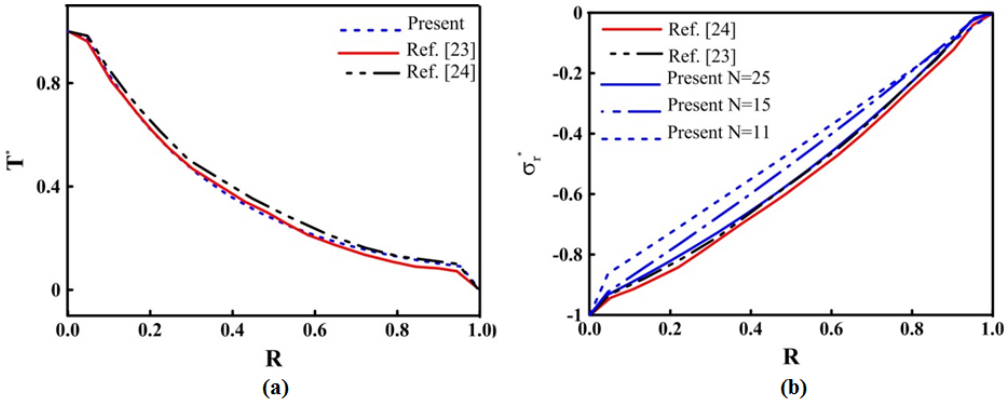

Fig. 2. (a) Temperature, (b) Radial stress.

Table 2
Verification of the results.

		R=0.2	R=0.4	R=0.6	R=0.8
T	Present	0.617453	0.352522	0.21255	0.127552
	Ref. 23	0.625014	0.367534	0.200022	0.107571
	Ref. 24	0.655038	0.395075	0.235015	0.135004
σ_r^*	Ref. 24	-0.85596	-0.67854	-0.48643	-0.24849
	Ref. 23	-0.83305	-0.66186	-0.46559	-0.22549
	N=25	-0.81844	-0.65554	-0.46144	-0.22341
	N=15	-0.78082	-0.59917	-0.39876	-0.19004
	N=11	-0.72653	-0.54704	-0.36953	-0.1858

Table 3
Effect of inhomogeneity index of actuator on the stresses and displacements at the midpoint of the shell.

	$S=5$			$S=10$			$S=15$		
	$\beta_i=-3$	$\beta_i=0$	$\beta_i=3$	$\beta_i=-3$	$\beta_i=0$	$\beta_i=3$	$\beta_i=-3$	$\beta_i=0$	$\beta_i=3$
σ_r^*	-1.034	-1.046	-1.071	-0.933	-0.941	-0.951	-0.907	-0.913	-0.920
σ_θ^*	-6.224	-5.783	-5.638	-5.992	-5.763	-5.599	-5.643	-5.496	-5.371
σ_z^*	-2.815	-0.566	0.366	-1.658	-0.776	-0.112	-1.368	-0.837	-0.372
$\tau_{rz}^*(\times 10^{-17})$	1.063	0.381	0.096	0.734	0.431	0.201	0.634	0.444	0.277
$u_r^*(\times 10^{-4})$	-1.831	-2.165	-2.347	-3.880	-3.975	-4.065	-4.585	-4.632	-4.682
$u_z^*(\times 10^{-19})$	-0.596	-0.994	-1.163	-0.815	-0.969	-1.086	-0.856	-0.948	-1.030

To illustrate the influence of inhomogeneity index of the perfectly bonded FGPM actuator on the stresses and displacements of the smart cylindrical shell, the shell was considered to be subjected to an inner pressure $P_i = 5$MPa and inner temperature and moisture concentration rise $T_a = 10$ and $M_a = 0.25$. Moreover, we have: $V = 200$, $K_L = 0$, $\beta_o = 0$ and $H^* = 0.8$ ($H = H* \times 0.22 \times 109$A/m). Table 3 shows the effect of the inhomogeneity index on the stresses and displacements for the middle point of the shell. It is observed that the stresses and displacements of the FGM layer can decrease or increase by selection of different inhomogeneity indexes for actuator. The minus value of i leads to decrease in the compressive radial stress as well as inward radial displacement, while, the effect of positive value of β_i is vice versa. Furthermore, the minus value of β_i leads to rise in the compressive hoop stress and transverse shear stress, whereas, the positive value of i has a reverse effect. It can be seen that the magnitude of changes is much greater for thick shells. Consequently, using FGPM actuator with proper inhomogeneity index is a way to reduce and control the stresses and displacements of the hybrid shell. It is worth mentioning that the multi-field equations of FGPM layers are nonlinear function of inhomogeneity index. Therefore, the multiphysical responses do not change with a specific trend by altering the inhomogeneity index. More investigation shows that the effect of inhomogeneity index of sensor layer (β_o) is not significant.

Effects of the hygrothermal loading on the stresses and radial displacement of the hybrid shell with different aspect ratio are presented in Fig. 3 and Table 4. For simplicity it is assumed that $\mathcal{X}_r^1 = \mathcal{X}_r^2 = 4\mathcal{X} \times 10^{-12}$, $\mathcal{X}_z^1 = \mathcal{X}_z^2 = \mathcal{X} \times 10^{-11}$, $\mathcal{X}_T^1 = \mathcal{X}_T^2 = 4\mathcal{X} \times 10^{-3}$ and $\mathcal{X}_C^1 = \mathcal{X}_C^2 = \mathcal{X} \times 10^{-6}$ we have $\beta_i = 4$ and $M_a = T_a/40$. It is observed from Fig. 3a and 3b that compressive radial stress and hoop stress of FGM layer increases by increasing the hygrothermal loading. The magnitude of the enhancement is higher for thick shell. Furthermore, the difference between hoop stresses of layers increases by increasing the hygrothermal loading. As shown in Fig. 3c, an increase in the

applied hygrothermal loading increases the inward radial displacement and this increase is nearer the inner surface of the shell. The magnitude of the enhancement is higher for thin shell. Fig. 3 implies that the existence of both humidity and thermal environmental conditions can extensively affect the stresses and displacements of a smart cylindrical shell. From Table 4, increase in the compliance coefficient of the imperfection results in the reduction of the absolute value of the hoop stress, as well as radial stress. The radial displacement of the FGM layer decreases by rising the compliance coefficient. The decline decreases by increasing $\mathcal{X}$.

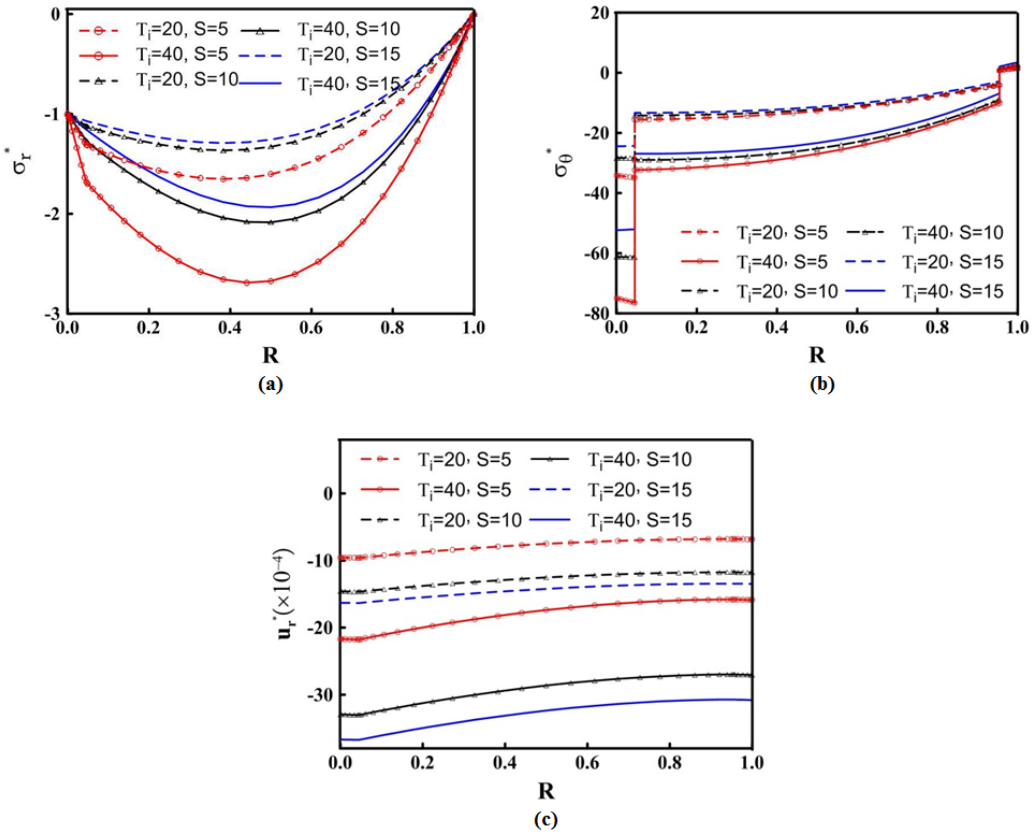

Fig. 3. Effect of hygrothermal loading and aspect ratio of the shell on the distribution of (a) Radial stress, (b) Hoop stress, (c) Radial displacement.

Table 4
Effect of imperfect bonding and aspect ratio of the shell on the stresses and displacements at the midpoint of the shell.

		$S=5$			$S=10$			$S=15$		
		$\mathcal{X}=0$	$\mathcal{X}=5$	$\mathcal{X}=10$	$\mathcal{X}=0$	$\mathcal{X}=5$	$\mathcal{X}=10$	$\mathcal{X}=0$	$\mathcal{X}=5$	$\mathcal{X}=10$
σ_r^*	T=20	-1.605	-1.160	-0.938	-1.329	-1.033	-0.891	-1.258	-0.993	-0.868
	T=40	-2.674	-1.836	-1.436	-1.510	-1.510	-1.241	-1.935	-1.414	-1.173
	T=60	-3.743	-2.512	-1.934	-2.842	-1.987	-1.591	-2.611	-1.834	-1.478
σ_θ^*	T=20	-12.758	-8.649	-6.946	-12.148	-9.197	-7.927	-11.370	-9.134	-8.162
	T=40	-26.998	-18.607	-15.062	-19.303	-19.303	-16.726	-23.369	-18.877	-16.915
	T=60	-41.238	-28.565	-23.179	-38.346	-29.410	-25.524	-35.368	-28.620	-25.668
σ_z^*	T=20	0.136	-0.073	-0.266	-0.271	-0.563	-0.678	-0.730	-0.852	-0.891
	T=40	-0.323	-0.536	-0.769	-1.119	-1.119	-1.302	-1.447	-1.656	-1.701
	T=60	-0.782	-1.000	-1.272	-0.908	-1.675	-1.925	-2.165	-2.459	-2.512
$\tau_{rz}^*(\times 10^{-17})$	T=20	0.358	0.055	-0.052	0.390	0.159	0.046	0.516	0.241	0.112
	T=40	0.883	0.268	0.046	0.322	0.322	0.111	0.994	0.456	0.209
	T=60	1.408	0.481	0.144	1.143	0.485	0.175	1.471	0.671	0.306
$u_r^*(\times 10^{-4})$	T=20	-6.831	-1.463	0.796	-11.385	-3.650	-0.323	-12.929	-4.585	-0.958
	T=40	-15.798	-4.875	-0.204	-10.468	-10.468	-3.733	-29.423	-12.683	-5.377
	T=60	-24.765	-8.288	-1.204	-40.667	-17.286	-7.142	-45.917	-20.780	-9.797
$u_z^*(\times 10^{-19})$	T=20	-2.267	-1.904	-1.732	-2.185	-1.886	-1.759	-2.064	-1.842	-1.749
	T=40	-4.475	-3.781	-3.461	-3.793	-3.793	-3.548	-4.134	-3.695	-3.514
	T=60	-6.683	-5.658	-5.189	-6.579	-5.700	-5.336	-6.204	-5.548	-5.279

The influences of a magnetic field on the behavior of a smart FG cylindrical shell is illustrated in Fig. 4. The shell was subjected to hygrothermo-electro-mechanical boundary condition as: $P_i = 5$MPa $V = 200$, $T_a = 10$, $k_L = 0$, $\beta_i = 3$ and $\beta_o = 0$. According to Fig. 4a, increasing the magnetic field leads to increase in the absolute value of the radial stress. This reduction is higher near the middle of the thickness of the shell. Fig. 4b depicts that the compressive hoop stress of FGM layer increases by increasing the magnetic field. Fig. 4c shows that the direction of the radial displacement can be reversed by applying a magnetic field. The outward radial displacement decreases by increasing the magnetic field. Higher magnetic field leads to change in the direction of the radial displacement. This inward radial displacement increases by increasing the magnetic field. Thus, the radial displacment of the shell can be minimized by considering a proper magnetic field.

It is valuale to explore the effect of magnetic field more carefully. The magnitude of the Lorentz force depends on the magnitude of magnetic field. In the pyroelectric materials there is an interaction between thermal, electric, and mechanical field. Each one of these fields can create stresses and displacements in the pyroelectric cylindrical shell. On the other hand, by existence of a magnetic field, the radial displacement results in creating the Lorentz force in the radial direction.

Fig. 5 shows the trend of variations in the stresses and displacements of middle point of the shell by increasing the applied magnetic field. As seen, the magnitude of variations increases by increasing the magnetic field. The radial and hoop stress increase by an increase in magnetic field. Moreover, the longitudinal and transverse shear stresses, as well as radial displacement, experience a change in sign by rising the magnetic field. Therefore, each of them can be vanished approximately by applying a proper magnetic field.

The effect of aspect ratio on the influence of magnetic field is demonstrated in Table 5. It shows that the magnitude of changes in stresses resulted by applying the magnetic field decreases by increasing the aspect ratio, while, this is vice versa for radial displacement. It means that applying a magnetic field is more effective on the stresses of thick shells, as well as radial displacement of thin shells.

Fig. 6 depicts that existence of imperfect bonding results in reduction of influence of applying a magnetic field on the stresses and radial displacement of the shell. So, the effect of bonding imperfection must be considered for accurate analysis of the multiphysical behavior of the hybrid shell.

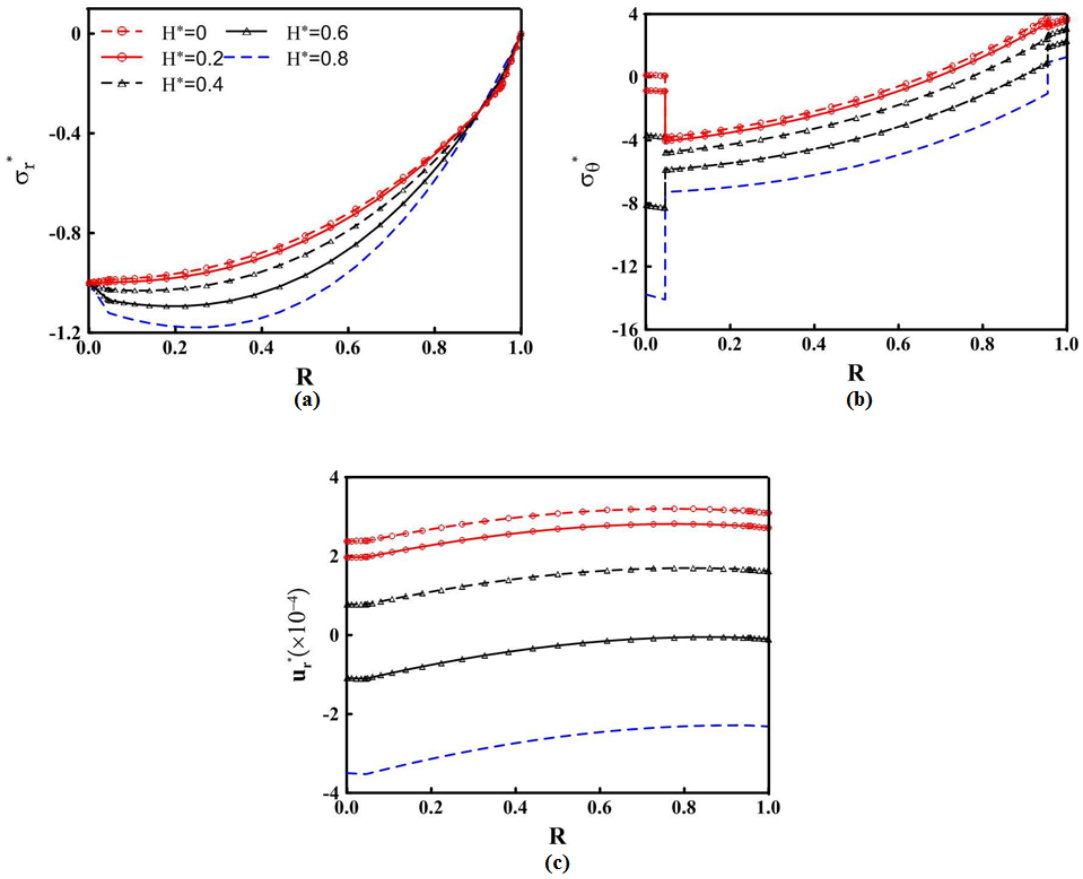

Fig. 4. Effect of magnetic field on the (a) Radial stress, (b) Hoop stress, (c) Radial displacement.

Table 5
Effect of magnetic field on the stresses and radial displacement at the midpoint of the shell.

	$S=5$			$S=10$			$S=15$		
	$H^*=0.2$	$H^*=0.6$	$H^*=1$	$H^*=0.2$	$H^*=0.6$	$H^*=1$	$H^*=0.2$	$H^*=0.6$	$H^*=1$
σ_r^*	-0.831	-0.970	-1.179	-0.716	-0.853	-1.056	-0.679	-0.819	-1.027
σ_θ^*	-1.733	-3.923	-7.613	-2.998	-4.437	-6.980	-3.497	-4.530	-6.377
σ_z^*	2.201	1.167	-0.548	0.306	0.067	-0.310	-0.155	-0.281	-0.470
$\tau_{rz}^*(\times 10^{-17})$	-0.453	-0.143	0.370	0.099	0.158	0.249	0.250	0.267	0.287
$u_r^*(\times 10^{-4})$	2.440	-0.241	-4.781	2.997	-0.895	-7.856	2.986	-1.224	-8.853
$u_z^*(\times 10^{-19})$	-1.274	-1.211	-1.108	-1.004	-1.048	-1.133	-0.951	-0.993	-1.074

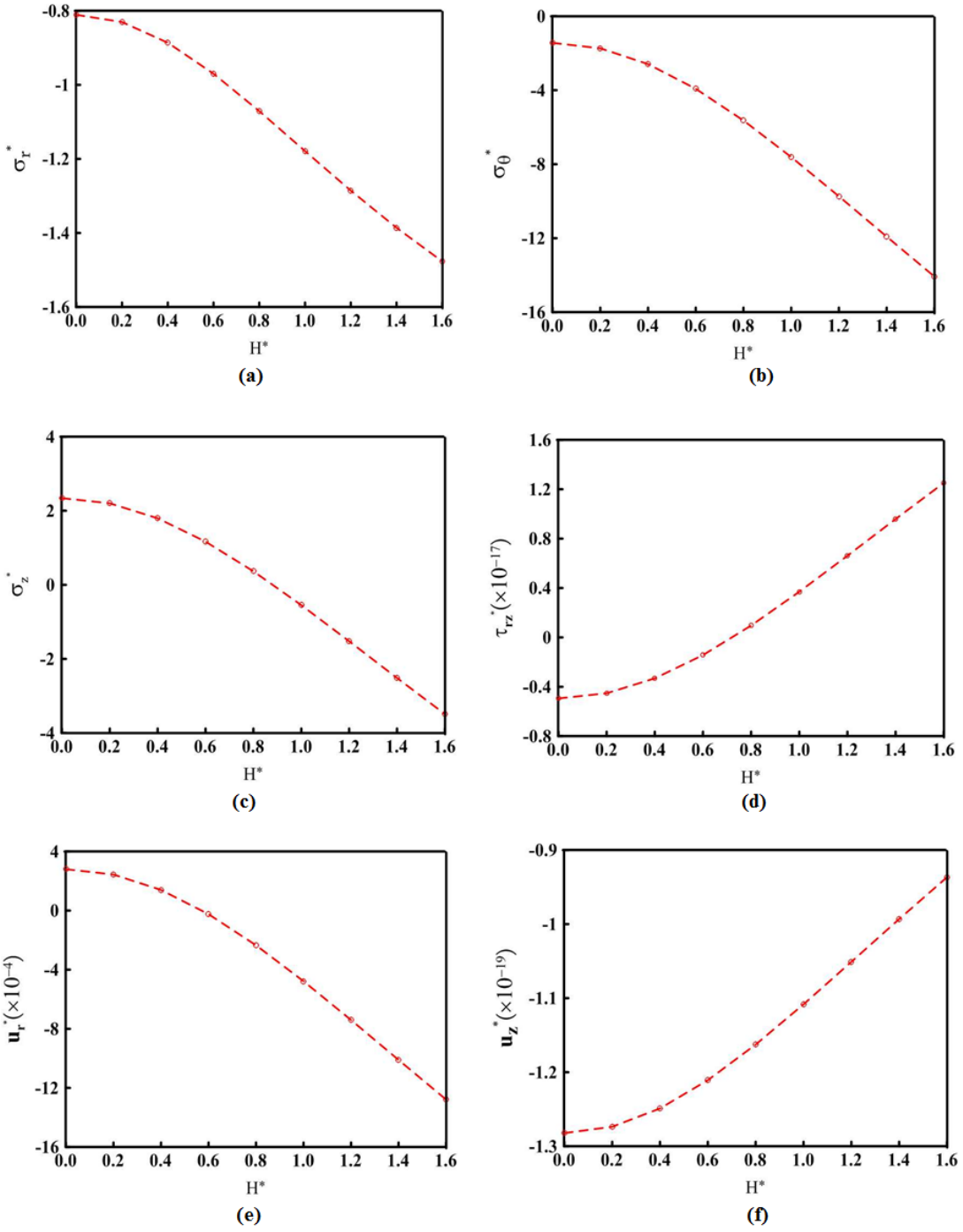

Fig. 5. Effect of magnetic field on the (a) Radial stress, (b) Hoop stress, (c) Longitudinal stress, (d) Transverse shear stress, (e) Radial displacement, (f) Longitudinal displacement of midpoint.

Fig. 7 depicts the effect of the elastic foundation on the radial stress and radial displacement of the hybrid shell. In this case, we have: $(K_L = k_L \times 10^{11})$. Fig. 7 shows in the case wherein the radial displacement is inward; due to the inward radial displacement, the presence of an elastic foundation helps to resist the radial displacement. This results in a tensile radial stress in the outer surface, as well as reduction in the radial displacement. It can be concluded that by changing the direction of the radial displacement, the elastic foundation causes a different effect on the behavior of the shell. In the case wherein the radial displacement is outward, unlike the former case, the existence of an elastic foundation helps to suppress the radial displacement and results in a compressive radial stress in the outer surface, as well as a reduction in the radial displacement. The rate of changes decreases by increasing k_L.

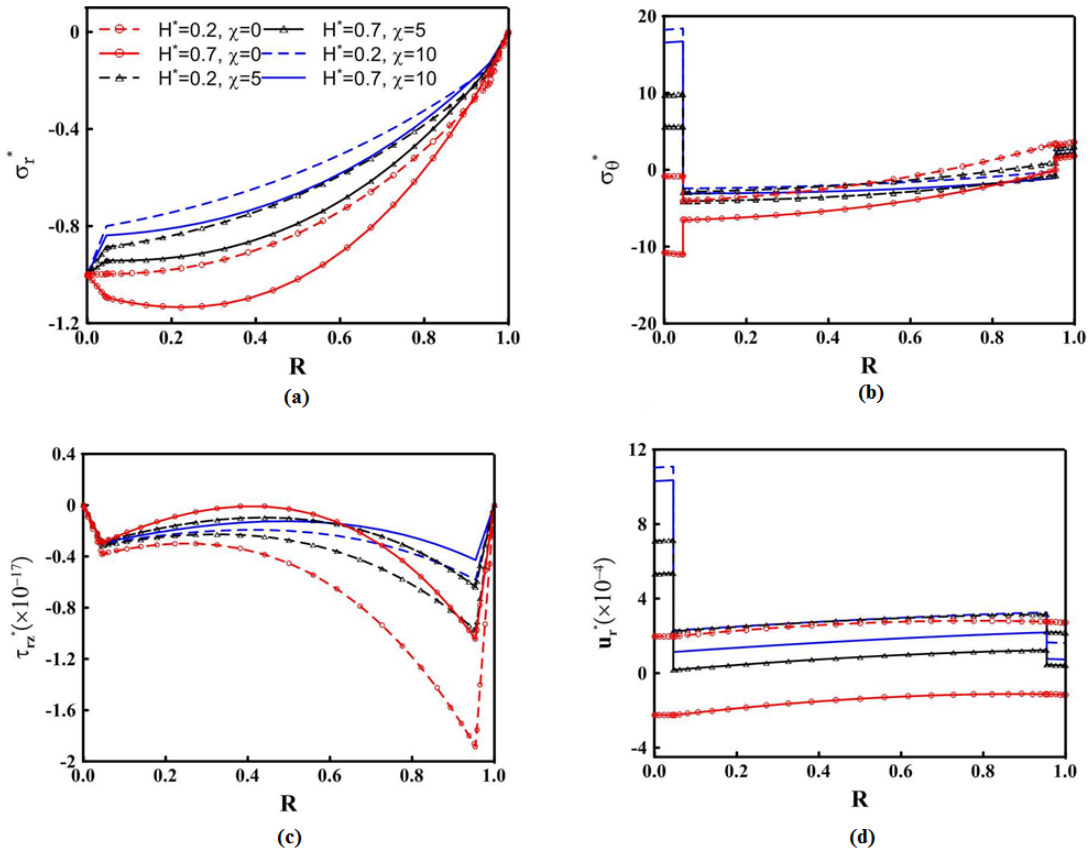

Fig. 6. Effect of magnetic field and imperfect bonding on the distribution of (a) Radial stress, (b) Hoop stress, (c) Transverse shear stress, (d) Radial displacement.

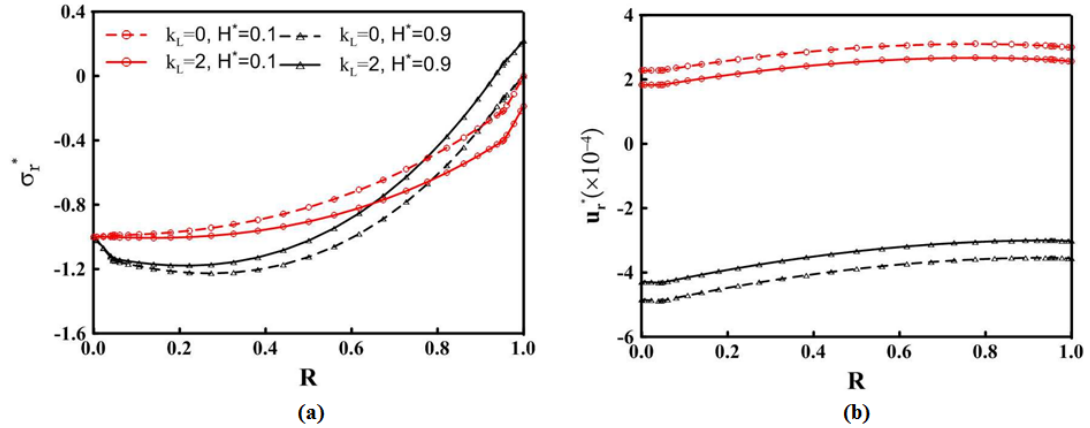

Fig. 7. Effect of elastic foundation on the distribution of (a) Radial stress, (b) Radial displacement.

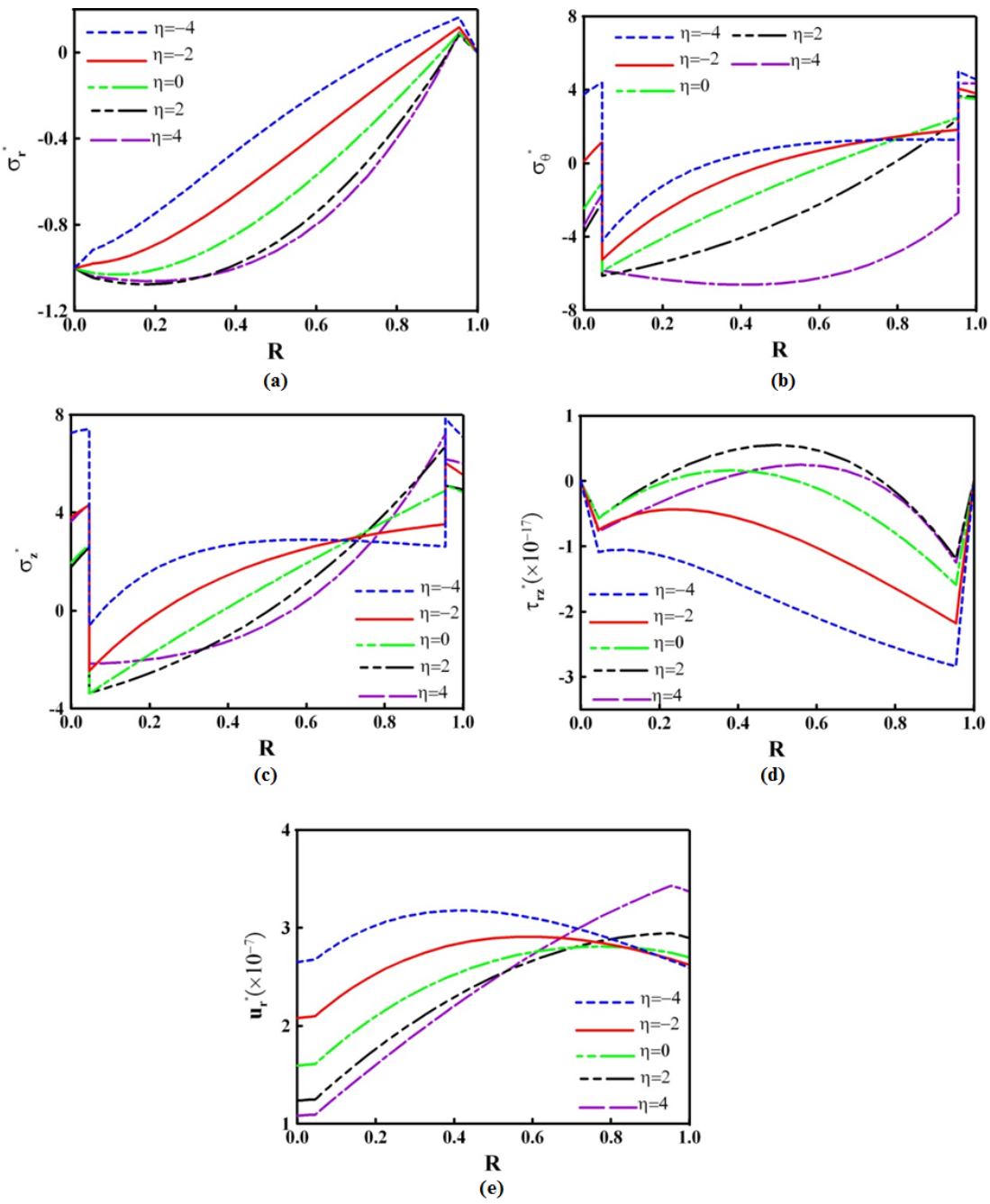

Fig. 8. Distribution of (a) Radial stress, (b) Hoop stress, (c) Longitudinal stress, (d) Transverse shear stress, (e) Radial displacement for different η.

The influence of the inhomogeneity index of the FGM layer on the behavior of the smart shell is shown in Fig. 8. In this case: $P_i = 6$MPa, $\beta_i = \beta_o = -5$, $V = 100$, $T_a = 10$, $M_a = 0.5$, $H^* = 0$, $K_L = 0$ and $\mathcal{X}$=0. The material properties of the inner surface of the FGM layer remain unchanged while $\eta = \eta_1 = \eta_2 = \eta_3 = \eta_4 = \eta_5 = \eta_6$. Other parameters and conditions remain unchanged.

Fig. 8a depicts that altering the inhomogeneity index from a minus value to a positive value results in an increase in the absolute value of the radial stress. Fig. 8b and c reveal that by altering the sign of the inhomogeneity index, the curvature of graphs turns vice versa. According to Fig. 8c and d, in the exterior surface of FGM, using positive inhomogeneity index leads to an increase in the longitudinal stress and a decrease in the transverse shear stress. While a negative inhomogeneity index has a reverse effect. Fig. 8e depicts that changing the inhomogeneity index from a minus value to a positive value results in a decrease in the radial displacement of the interior surface of the hybrid shell, as well as an increase in the radial displacement of the exterior surface.

5. Conclusions

The static multiphysical behavior of a functionally graded hollow cylindrical shell with the inner and the outer surface imperfectly bonded functionally graded piezoelectric sensor and actuator subjected to multi-field loads was numerically analyzed by using a series type solution and the DQ method. The hybrid shell was placed in a constant magnetic field and subjected to hygrothermo-electro-mechanical loads. The material properties of each layer were assumed to be graded in the radial direction according to the power law function. The following conclusions were obtained:

- The inhomogeneity index of the FGPM actuator has a considerable effect on its authority. Moreover, the magnitude and even sign of stresses and displacements in the FGM layer can be controlled more effectively by using the FGPM actuator and sensor with a suitable gradient index. The effect of the inhomogeneity index of the outer FGPM layer on the temperature and moisture concentration distribution is more distinctive.

- The results imply that the simultaneous existence of humidity and thermal environmental conditions can severely affect the behavior of a smart cylindrical shell.

- The actuation authority and sensory potentials of the FGPM layers are significantly affected by the presence of bonding imperfections. Increasing the compliance coefficient of the imperfection shows reduction in the actuation capability of the actuator as well as the measured sensor voltage.

- In multifield loading, for a certain electro-magneto-thermo-mechanical conditions, there exists certain points within the thickness at which the transverse shear stress is independent of the hygrothermal condition.

- By increasing the magnetic field, the radial stress decreases and hoop stress increases. Furthermore, the direction of the radial displacement can be reversed by increasing the magnetic field.

- The results obtained can be used for designing hybrid FG structures subjected to multi-filed loadings in multiphysical environmental conditions.

References

[1] A.S. De Paula, D.J. Inman, M.A. Savi, Energy harvesting in a nonlinear piezomagnetoelastic beam subjected to random excitation, Mech. Sys. Signal Proc., 54-55 (2015) 405-416.

[2] G.L.C.M. Abreu, G.P.D. Melo, J.V. Lopes, M.J. Brennan, Active modal damping control of a smart truss structure using a self-organizing fuzzy controller, J. Braz. Soc. Mech. Sci. Eng., 37(2) (2015) 441-450.

[3] K. Nguyen-Quangad, H. Dang-Trungab, V. Ho-Huu, H. Luong-Van, T. Nguyen-Thoi, Analysis and control of FGM plates integrated with piezoelectric sensors and actuators using cell-based smoothed discrete shear gap method (CS-DSG3), Compos. Struct., 165 (2017) 115-129.

[4] M. Saadatfar, S.A. Razavi, Piezoelectric hollow cylinder with thermal gradient, J. Mech. Sci. Tech., 23(1) (2009) 47-55.

[5] M. Saadatfar, A. Rastgoo, Stress in piezoelectric hollow sphere with thermal gradient, J. Mech. Sci. Tech., 22(8) (2008) 1460-1467.

[6] A.M. Zenkour, M.N.M. Allam, A.F. Radwan, Effects of hygrothermal conditions on cross-ply laminated plates resting on elastic foundations, Arch. Civil Mech. Eng., 14 (2014) 144-159.

[7] W. Smittakorn, P.R. Heyliger, An adaptive wood composite: Theory, Wood. Fiber. Sci., 33(4) (2001) 595-608.

[8] M. Saadatfar, M. Aghaie-Khafri, Hygrothermo-magnetoelectroelastic analysis of a functionally graded magnetoelectroelastic hollow sphere resting on an elastic foundation, Smart. Mater. Struct., 23(3) (2014) 035004.

[9] A.M. Zenkour, Hygro-thermo-mechanical effects on FGM plates resting on elastic foundations, Compos. Struct., 93(1) (2010) 234-238.

[10] M.S.A. Houari, A. Tounsi, O. Anwar Beg, Thermoelastic bending analysis of functionally graded sandwich plates using a new higher order shear and normal deformation theory, Int. J. Mech. Sci., 76 (2013) 102-111.

[11] H. Bellifa, K.H. Benrahou, L. Hadji, M.S.A. Houari, A. Tounsi, Bending and free vibration analysisof functionally graded plates using a simple shear deformation theory and the concept the neutral surface position, J. Braz. Soc. Mech. Sci., 38(1) (2018) 265-275.

[12] A. Bakhshizadeh, M. Zamani Nejad, M. Davoudi Kashkoli, Time-dependent hygro-thermal creep analysis of pressurized fgm rotating thick cylindrical shells subjected to uniform magnetic field, J. Solid. Mech., 9(3) (2017) 663-679.

[13] M. Sobhy, M.S. Alotebi, Transient hygrothermal analysis of fg sandwich plates lying on a visco-pasternak foundation via a simple and accurate plate theory, Arab J. Sci. Eng., 43(10) (2018) 5423-5437.

[14] M. Smittakorn, P.R. Heyliger, A discrete-layer model of laminated hygrothermopiezoelectric plates, Mech. Compos. Mater. Struct., 7(1) (2000) 79-104.

[15] A.M. Zenkour, Hygrothermoelastic responses of inhomogeneous piezoelectric and exponentially graded cylinders, Int. J. Pres. Ves. Pip., 119 (2014) 8-18.

[16] X. Wang, K. Dong, X.Y. Wang, Hygrothermal effect on dynamic interlaminar stresses in laminated plates with piezoelectric actuators, Compos. Struct., 71(2) (2005) 220-228.

[17] P.K. Mahato, D.K. Maiti, Aeroelastic analysis of smart composite structures in hygro-thermal environment, Compos. Struct., 92(4) (2010) 1027-1038.

[18] A.H. Akbarzadeh, Z.T. Chen, Hygrothermal stresses in one-dimensional functionally graded piezoelectric media in constant magnetic field, Compos. Struct., 97 (2013) 317-331.

[19] A.M. Zenkour, Hygrothermal analysis of heterogeneous piezoelectric elastic cylinders, Math. Model. Eng., 2(1) (2016) 1-17.

[20] M. Saadatfar, M. Aghaei-Khafri, Hygrothermal analysis of a rotating smart exponentially graded cylindrical shell with imperfect bonding supported by an elastic foundation, Aerosp. Sci. Technol., 43 (2015) 37-50.

[21] R. Talebitooti, K. Daneshjou, A. Tarkashvand, Study of imperfect bonding effects on sound transmission loss through functionally graded laminated sandwich cylindrical shells, Int. J. Mech. Sci., 133 (2017) 469-483.

[22] M. Saadatfar, M. Aghaei-Khafri, Electromagnetothermoelastic behavior of a rotating imperfect hybrid functionally graded hollow cylinder resting on an elastic foundation, Smart. Struct. Sys., 15(6) (2015) 1411-1437.

[23] A. Alibeigloo, Thermoelastic solution for static deformations of functionally graded cylindrical shell bonded to thin piezoelectric layers, Compos. Struct., 93(2) (2011) 961-972.

[24] R. Akbari Alashti, M. Khorsand, Three-dimensional thermo-elastic analysis of a functionally graded cylindrical shell with piezoelectric layers by differential quadrature method, Int. J. Pres. Ves. Pip., 88(5-7) (2011) 167-180.

[25] M. Saadatfar, M. Aghaei-Khafri, On the magneto-thermo-elastic behavior of a functionally graded cylindrical shell with pyroelectric layers featuring interlaminar bonding imperfections rested in an elastic foundation, J. Solid. Mech., 7(3) (2015) 344-363.

[26] M. Saadatfar, M. Aghaei-Khafri, Thermoelastic analysis of a rotating functionally graded cylindrical shell with functionally graded sensor and actuator layers on an elastic foundation placed in a constant magnetic field, J. Intell. Mater. Syst. Struct., 27(4) (2016) 512-527.

[27] M. Saadatfar, M. Aghaei-Khafri, On the behavior of a rotating functionally graded hybrid cylindrical shell with imperfect bonding subjected to hygrothermal condition, J. Thermal. Stresses., 38(8) (2015) 854-881.

[28] A. Alibeigloo, Thermoelastic analysis of functionally graded carbon nanotube reinforced composite cylindrical panel embedded in piezoelectric sensor and actuator layers, Compos. Part B: Eng., 98 (2016) 225-243.

[29] M. Shaban, A. Alibeigloo, Global bending analysis of corrugated sandwich panels with integrated piezoelectric layers, J. Sandwich. Struc. Mater., (2018) https://doi.org/10.1177/1099636218780172.

[30] M. Saadatfar, Effect of multiphysics conditions on the behavior of an exponentially graded smart cylindrical shell with imperfect bonding, Meccanica, 50(8) (2015) 2135-2152.

[31] S.H. Chi, Y.L. Chung, Mechanical behavior of functionally graded material plates under transverse load-Part I: Analysis, Int. J. Solid. Struct., 43(13) (2006) 3657-3674.

[32] M. Bhandari, K. Purohit, Analysis of functionally graded material plate under transverse load for various voundary conditions, IOSR J. Mech. Civil Eng., 10 (2014) 46-55.

[33] S. Rohit, P.R. Maiti, Buckling of simply supported FGM plates under uniaxial load, Int. J. Civ. Struct. Eng., 2(4) (2012) 1035-1050.

[34] R. Ansari, M. Darvizeh, Prediction of dynamic behavior of FGM shells under arbitrary boundary conditions, Compos. Struct., 85(4) (2008) 284-292.

[35] W. J. Chang, Transient hygrothermal responses in a solid cylinder by linear theory of coupled heat and moisture, Appl. Math. Model., 18(8) (1994) 467-473.

[36] J.D. Kraus, Electromagnetic, McGraw-Hill, New York, (1984).

[37] G. Paria, Magneto-elasticity and magneto–thermo-elasticity, Adv. Appl. Mech., 10 (1967) 73-112.

[38] A.H. Akbarzadeh, D. Pasini, Multiphysics of multilayered and functionally graded cylinders under prescribed hygrothermomagnetoelectromechanical loading, J. Appl. Mech., 81(4) (2014) 041018-1-041018-15.

[39] C. Shu, Differential quadrature and its application in engineering, Springer Publication, New York, (2000).